

L. Voigt, J. Heinze, M. Korkmaz, K.P. Geigle, C. Willert
Planar measurements of CO concentrations in flames at atmospheric and
elevated pressure by laser-induced fluorescence, Appl. Phys. B 125:71 (2019)

The original publication is available at www.springerlink.com

<http://dx.doi.org/10.1007/s00340-019-7181-4/>

Planar measurements of CO concentrations in flames at atmospheric and elevated pressure by laser-induced fluorescence

Lena Voigt¹, Johannes Heinze¹, Metin Korkmaz², Klaus Peter Geigle³, Chris Willert¹

1	2	3
Institute of Propulsion Technology German Aerospace Center (DLR) Linder Hoehe 51147 Cologne, Germany Lena.Voigt@dlr.de phone: +49 2203 601 2145 fax: +49 2203 64395 Johannes.Heinze@dlr.de phone: +49 2203 601 2221 Chris.Willert@dlr.de phone: +49 2203 601 2308	Institute for Combustion Technology RWTH Aachen University Templergraben 64 52062 Aachen, Germany M.Korkmaz@itv.rwth-aachen.de phone: +49 241 80 - 94877 fax: +49 241 80 - 92923	Institute of Combustion Technology German Aerospace Center (DLR) Pfaffenwaldring 38-40 70569 Stuttgart, Germany Klauspeter.Geigle@dlr.de phone: +49 711 6862 - 398 fax: +49 711 6862 - 578

Abstract

The article describes the development and application of a laser-optical technique for the quantitative measurement of carbon monoxide (CO) in combustion environments of elevated pressures relevant of gas turbine environments. Planar CO measurements can provide important information for the understanding of several aspects of the combustion process, such as localized lean blowout conditions or quenching effects of effusion cooling on the combustor flow. While laser-induced fluorescence (LIF) is a sensitive non-intrusive measuring technique suitable for planar detection, the CO molecule cannot be excited directly in the visible or near UV. For the present implementation, a two-photon excitation scheme with resulting fluorescence in the visible range is utilized. To qualify the technique, planar measurements in a laminar premixed atmospheric flame are performed in a first step; this flame is later on used for calibration of CO concentrations in a laminar premixed flame at elevated pressure

up to 5 bar and in a generic turbulent combustor with a swirl-stabilized flame operated at atmospheric pressure. Pressure effects on spectral structures and the calibration procedure are discussed, as well as potential interference by cross sensitivity with other species. Based on this optimization strategies are defined for the respective experimental arrangements.

Introduction

The detection of carbon monoxide (CO) is of great interest in different fields of research. Especially in reactive flows, knowledge of spatially and temporally resolved CO concentrations is important for the understanding of the combustion process and for the validation of the appropriate numerical calculation methods. CO oxidation provides most of the combustion energy in hydrocarbon combustion. Modern gas turbine (GT) combustors are designed to work as lean as possible to minimize NO_x emissions. Near lean blowout can result in a delay or

interruption of the reaction, resulting in increased CO emissions. On this basis, CO can be an important indicator of the quality of combustion. Beyond this, the emission levels of CO as a long-lived, toxic gas are strictly regulated in almost all countries [1]. Knowledge of the location and the temporal behavior of CO formation and oxidation are therefore essential for the achievement of low emission levels which motivates a great interest in in-situ CO diagnostics.

Among the non-intrusive measurement techniques, laser-induced fluorescence (LIF) is an optical method with both a high sensitivity as well as high spatial and temporal resolution [2, 3]. When used as a planar technique, CO PLIF provides spatial correlations in a plane. Unfortunately, CO [4] is one of the molecules such as N₂, H₂, CO₂, or H₂O [5], which cannot be directly excited electronically by visible or UV light, but requires vacuum-UV excitation (VUV). However, excitation wavelengths in the VUV are of no practical use at GT-relevant combustion chamber pressures, because VUV radiation is immediately absorbed by the optically dense medium. Likewise, the planar infrared LIF excitation and emission scheme [6, 7, 8] is no promising alternative under these conditions either, due to strong IR luminosity of hot high pressure flames. In contrast, the use of a 2-photon transition in the UV is very promising for LIF applications. One of the most common excitation wavelengths is at 230 nm using excitation in the Hopfield-Birge system ($B^1\Sigma^+ \leftarrow\leftarrow X^1\Sigma^+$) with resulting fluorescence in the Ångström bands of the $B^1\Sigma^+ \rightarrow A^1\Pi_u$ transition in the visible range (450-670 nm). This LIF scheme has also been presented in early publications on CO-LIF application to flames by Loge et al. [9] or Alden et al. [10], and has been studied in more detail to determine important parameters of this 2-photon transition, such as 2-photon absorption and photoionization cross sections, pressure broadening and

shifting, as well as quenching rate [11, 12, 13, 14]. Compared to other transitions, like the 3rd positive band (290-370 nm), the Ångström band offers the advantage of a lower pressure dependence, which allows use at higher pressures [15]. Compared to the alternative CO detection after $C^1\Sigma^+ \leftarrow\leftarrow X^1\Sigma^+$ 2-photon excitation at 217 nm with resulting fluorescence in the Herzberg bands of the $C^1\Sigma^+ \rightarrow A^1\Pi_u$ transition in the near UV and visible range (360-530 nm), CO detection upon 230 nm-excitation is advantageous, because of its excitation spectrum with lower line density, no pre-dissociation and a more efficient generation of the excitation wavelength by adequate laser systems. The experiments described above were performed with ns laser system. To increase substantially the pulse power, Li et al. [16], Richardson et al. [17] and Rahman et al. [18] recently made use of fs laser systems for the two-photon CO excitation scheme at 230 nm. The pulse durations of 45 fs and 100 fs respectively have the additional advantage to be short enough to avoid the excitation of photolytic generated products like C₂. However, the fs laser pulses have a Fourier-limited spectral bandwidth much larger than the entire CO excitation spectrum and a limited pulse energy despite high experimental effort.

The aim of this paper is to demonstrate feasibility to measure planar CO distributions using the Hopfield-Birge transition at 230 nm in turbulent flames at elevated pressure. In order to provide sufficient laser pulse energy and power for 2-photon planar LIF with good S/N ratio and spectral resolution, an efficient generation scheme of pulsed narrowband ns UV laser radiation at 230 nm with high short and long term stability is presented. The fluorescence spectra of the CO $B \leftarrow\leftarrow X$ excitation, their laser power dependence and the spectral interference of the CO LIF bands with those of C₂ are examined. To do so, experiments in laminar premixed flames are

performed at pressures up to 5 bar, and their results are interpreted using simulated spectra for comparison. A calibration scheme of the CO 2-photon PLIF images for determination of quantitative CO concentrations is presented and experimentally verified by systematic variation of equivalence ratio and pressure of the flame. Finally, the CO PLIF measurement technique is applied to a generic model combustor, and the CO concentration distributions of turbulent swirl-stabilized flames of different equivalence ratios are determined and discussed.

Theory

A short outline of modelling the CO 2-photon excitation spectrum is given to show the influence of the spectroscopic and environmental parameters on the measured spectra, such as laser pulse energy, temperature, pressure, and gas composition. In addition, the calculation also allows the optimization of measurement strategies, such as finding a temperature insensitive excitation line for specific gas compositions present in the experiment.

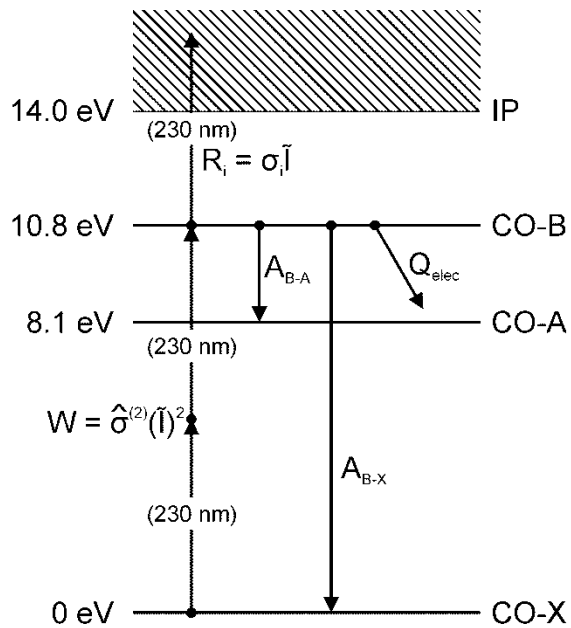


Figure 1: Energy diagram with processes relevant to CO detection through two-photon excitation of $B \leftarrow X$ [14].

As basis of this calculation, a simple four-level model similar to that in [19] is used. The corresponding energy diagram of the four involved electronic states of the CO molecule is schematically shown in Figure 1. Here, all finer rotational-vibrational structures are considered only indirectly. The electronic ground state X of CO is excited to the B state by the 2-photon transition. This electronically excited-B state can relax into the A state or the electronic ground state X at a spontaneous fluorescence rate A or by non-fluorescent collisions, i.e. by quenching (Q_{elec}). In addition, the B state can be ionized by absorbing another photon.

The 2-photon excitation rate W of the B-X transition can be written as the product of 2-photon-excitation cross section $\hat{\sigma}^{(2)}$ and the square of the photon flux density \tilde{I} [14]. Therefore, a high photon flux density with sufficient coherence is essential for a high 2-photon excitation rate. The radiative decay of the excited B state takes place with the fluorescence rate A_{B-A} into the CO A state; this transition is selected for fluorescence in the visible spectral range later on. In addition, the decay rates by VUV fluorescence into the ground state and the environment-depending quenching are given by A_{B-X} and Q_{elec} , respectively. Although the quenching rate Q_{elec} is significantly higher than the fluorescence rates A at the studied experimental conditions of 1–5 bar, the photoionization with rate R_i substantially contributes to the depletion of the CO B state. The ionization process even becomes dominant at photon flux densities \tilde{I} , which are convenient for 2-photon CO PLIF experiments. At these photon flux densities, the CO 2-photon PLIF becomes independent of the composition-dependent quenching.

The laser-induced fluorescence rate R_f [$\text{cm}^{-3} \text{s}^{-1}$] can be written as product of the number density N_{CO} [cm^{-3}] of the probed CO quantum

state, the excitation rate W [s^{-1}] and the fluorescence quantum yield η [19]:

$$R_f = N_{CO} \cdot W \cdot \eta \quad (1)$$

Following the example of Saxon and Eichler [20] the excitation rate W [s^{-1}] is expressed as

$$W = \hat{\sigma}^{(2)} \cdot \tilde{I}^2 \quad (2)$$

with $\hat{\sigma}^{(2)}$ in [cm^4s] and \tilde{I} in [$cm^{-2}s^{-1}$].

The rate coefficient $\hat{\sigma}^{(2)}$ at the laser frequency ω_L or at the 2-photon frequency Ω_L is defined by the following equation:

$$\begin{aligned} \hat{\sigma}^{(2)}(2\omega_L) &= \hat{\sigma}^{(2)}(\Omega_L) \quad (3) \\ &= \sigma_0^{(2)} \cdot G^{(2)} \cdot \sum_{J''} F_{J''} \cdot \sum_{J'} S_{J'J''}^{(2)} \\ &\quad \times \int_{-\infty}^{\infty} \Phi_{J'J''}(\xi - \Omega_{J'J''}) \cdot g'(\xi - \Omega_L) d\xi \end{aligned}$$

$\sigma_0^{(2)}$ [cm^4] denotes the spectrally integrated 2-photon cross section [14], $F_{J''}$ is the Boltzmann fraction of the rotational level J'' , and $S_{J'J''}^{(2)}$ is the Hönl-London factor of the 2-photon transition $J'J''$ at frequency $\Omega_{J'J''}$. The spectral line shape $\Phi_{J'J''}(\Omega)$ of the molecular transition is the convolution of the homogenous and inhomogeneous line broadening, with the main contributions given by pressure and Doppler broadening. Here $g(\Omega)$ is the spectral laser profile. As usual, all functions $\Phi_{J'J''}(\Omega)$ and $g(\Omega)$, as well as $S_{J'J''}^{(2)}$ are normalized. The second-order intensity correlation factor [21] $G^{(2)}$ of the exciting laser is assumed to be $G^{(2)} \approx 2$, assuming a temporally chaotic photon statistics during the laser pulse [22].

The fluorescence quantum yield η is calculated by the Stern-Volmer equation [19]:

$$\eta = \frac{A_{B-A}}{A_{total} + Q_{elec} + R_i} \quad (4)$$

with A_{B-A} or A_{total} denoting the specific spontaneous emission rate, and R_i the photoionization rate. The total quenching rate Q_{elec} is calculated as the sum of the relative contributions $n_k C_k$ of the gas components k , scaling with pressure p :

$$Q_{elec} = p \cdot \sum_k n_k C_k \quad (5)$$

The calculation of the fluorescence rate $R_f(\omega)$ is performed by a simulation and non-linear fit program [23, 24], which has been extended for the specific equations of the 2-photon transition. The rotational transition frequencies $\Omega_{J'J''}$ of the CO B-X (0, 0) transitions are calculated using the molecular constants of Le Floch [25] to derive the rotational vibrational levels for the CO X ground state, and those of Eidelsberg et al. [26] are used for the CO B state levels. When exciting a 2-photon transition by linearly polarized light, the Q branch is the dominant one, while contributions of the O and S branches are neglected [27]. Therefore the rotational line strength $S_{J'J''}^{(2)}$ is chosen as $S_{J'J''}^{(2)} = 1$ for $J'=J''$. To calculate the spectral line shape $\Phi_{J'J''}$ of the rotational transition, pressure broadening and pressure shift are taken into account. The corresponding coefficients of Di Rosa and Farrow [12] are used - the missing values for the collisional partners CO_2 and O_2 were substituted by the values for H_2O and the average of the values for N_2 and O_2 respectively, weighted by the exhaust gas composition. For flame conditions up to 5 bar examined in this paper, Lorentz line shape profiles are proven to be optimal to describe pressure broadening and shift effects, while the asymmetric Lindholm line shape profile [28] is the better choice at room temperature [29]. The subsequent convolution with the Doppler profile and the laser profile as a Voigt profile leads to the final spectrum.

Quenching rates are calculated using the coefficients of Settersten et al. [13]. The exhaust gas composition n_k is determined using the GasEq program [30]. The photoionization rate can be written as the product of photon flux \tilde{I} and the ionization cross section $\sigma_i^{J'}$:

$$R_i = \sigma_i^{J'} \cdot \tilde{I} \quad (6)$$

The dependence of the ionization cross-section on the rotational line J' is taken into account [11] and will be discussed later.

The laser-induced fluorescence flux I_{LIF} , detected by the camera system, is proportional to the part $\Omega/4\pi$ of the laser-induced fluorescence rate R_f , captured by the solid angle Ω of the camera lens. Additionally, if a spectral filter is used to discriminate spectral interferences by other species, as shown in Figure 7, only part of the total fluorescence $a_f = A_f/A_{B-A}$ reaches the ICCD camera, which has a detection efficiency ξ . Using the equations (1) – (4), the measured LIF flux I_{LIF} can be written as

$$I_{LIF} = R_f \cdot a_f \cdot \frac{\Omega}{4\pi} \cdot \xi = N_{CO} \cdot \hat{\sigma}^{(2)} \tilde{I}^2 \cdot \frac{a_f \cdot A_{B-A}}{A_{total} + Q_{elec} + R_i} \cdot \frac{\Omega}{4\pi} \cdot \xi \quad (7)$$

In a non-linear least squares fit routine applied to the experimental spectrum, temperature, the laser line width or other parameters of the calculated spectrum can be determined [23, 24].

To achieve a sufficient 2-photon CO PLIF signal, the laser flux density \tilde{I} , the spectral LIF filtering a_f , the solid angle Ω or F-number of the lens, and the detection efficiency ξ of the ICCD camera have to be optimized, as described in the following section.

Experimental setup

Analysis of the CO signal using a spectrometer

To obtain a good CO PLIF signal via the 2-photon excitation at 230 nm, laser light of sufficient pulse energy and intensity is necessary. An efficient generation scheme of tunable laser light at 230 nm is sum frequency mixing (SFM) of the third harmonic (355 nm) of the Nd:YAG laser and the fundamental (654 nm) of a dye laser mixed in a BBO crystal. This requires just one mixing process of two comparatively stable laser light sources. For the present setup, a Nd:YAG laser (Spectra-Physics Quanta Ray; Pro-230-10 Hz) is used both for pumping a tunable dye laser (Sirah, Cobra-Stretch-LG-24) at 532 nm, and subsequent mixing of its 3rd harmonic with the dye laser radiation. The harmonic generator of the Nd:YAG laser is operated such that the simultaneous use of the 2nd and the 3rd harmonic in a well-balanced intensity ratio of 3 : 1 is possible. The Nd:YAG laser is equipped with a cw single-mode seed laser (Spectra Physics Model 6350) to achieve a Fourier limited bandwidth of 3rd harmonic for the subsequent SFM in the frequency conversion unit (FCU) of the dye laser.

Using a solution of DCM dye in the solvent DMSO, pumped at 532 nm, narrow-band laser light of less than 0.002 nm line width is generated at a wavelength close to 654 nm. The subsequent SFM process of the dye laser emission and the Fourier limited 3rd harmonic of the Nd:YAG laser yields a resulting bandwidth of 0.0002 nm at 230 nm, which is substantially below the CO molecular line width, even at atmospheric pressure. Such a narrow laser linewidth of $\leq 0.05 \text{ cm}^{-1}$ was achieved under good experimental conditions of atmospheric CO experiments in the laboratory, as shown in the results section,

Figure 15. The laser linewidth was determined by fitting the calculated CO spectra to the measured one. Under the harsher test conditions of the high-pressure test rig, a larger effective laser linewidth of $\leq 0.08 \text{ cm}^{-1}$ or 0.0004 nm at 230 nm was determined. The laser system provides up to 130 mJ for the wavelength 654 nm and 100 mJ at 355 nm prior to frequency mixing. For the separation of the initial wavelengths from the resulting wavelength close to 230 nm , dielectric mirrors are used rather than Pellin-Broca prisms. At the exit of the mixing unit, a power of up to 30 mJ at 230 nm is measured, with good pulse-to-pulse and long term stability. The SFM generation scheme yields a pulse-to-pulse stability of 3% which is about a factor of 1.5 smaller than the SHG pulse-to-pulse stability of typically 4.5% . Additionally, the use of DCM dye enables stable laser pulse energies over several weeks of laser operation.

To determine the absolute wavelength of both the Nd:YAG laser and the dye laser, a wavelength meter (High Finesse, model WSU/10) is used. First, the wavelength of the seeded Nd:YAG laser is determined by measuring its second harmonic. Then, during excitation spectra measurements, an optical fiber couples a small part of the dye laser beam into the wavelength meter, which is calibrated with a HeNe laser. All wavelengths refer to vacuum conditions to allow easy conversion into energy units like wavenumbers.

The light sheet optics slightly differs depending on the experimental task. For high laser intensity experiments the laser beam of 4 mm diameter is directly focused by a cylindrical lens ($f = 310 \text{ mm}$) to achieve a maximal power density of 1 GW/cm^2 (Figure 13 and Figure 15) within the focus of $40 \mu\text{m}$ thickness ($M^2 = 1.7$). For all other experiments a light sheet is formed by expanding the laser

beam using a -200 mm cylindrical lens and a spherical lens ($+500 \text{ mm}$). This results in a light sheet of 10 mm width and approximately $60 \mu\text{m}$ thickness of the beam waist. The light sheet optics lead to moderate laser power densities of about $0.1 - 0.2 \text{ GW/cm}^2$ within the focus. This experimental setup was used for nearly all other shown CO spectra and PLIF images. The laser intensities of both laser light sheet optics are marked in the diagram on the influence of the photon flux on the 2P-LIF signal in Figure 13 of the results section.

The light sheet for spectrally resolved acquisition is aligned parallel to the matrix of the atmospheric burner at a distance of 15 mm , to integrate the signal over the depth of the sheet (see Figure 2 and Figure 3). This yields a high and stable signal at laser intensities comparable to those used in the planar CO measurements later on.

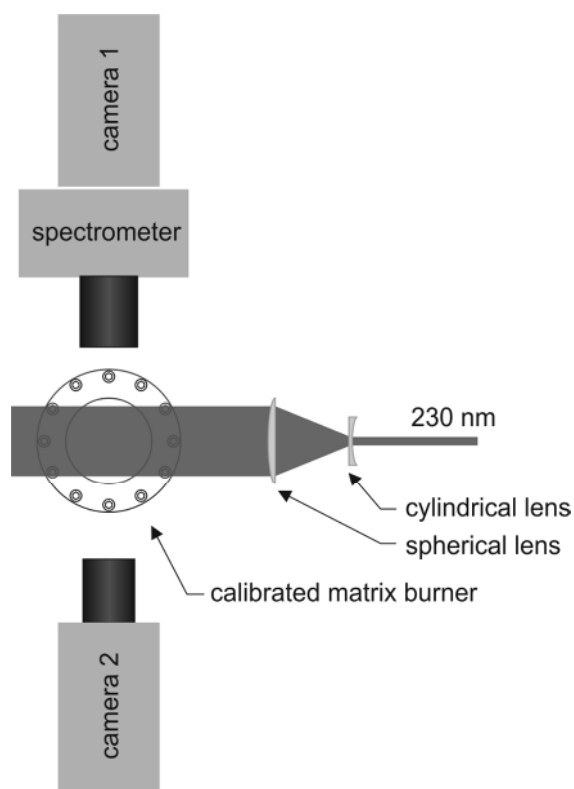


Figure 2: Top view of setup for spectral analysis of the CO fluorescence signal with the light sheet parallel to the face of the matrix burner.

For recording of the spatially resolved emission spectra, a spectrometer (SpectraPro

275, Acton Research Corporation, aperture ratio $f/3.8$) is arranged in front of a matrix burner such that the entrance slit is oriented parallel to the laser beam. This allows to image the fluorescence over a length of about 28 mm along the laser focus with the scale 1:2.4, using an achromatic lens (UV Nikkor $f=105$ mm, $f/4.5$), onto the entrance slit of the spectrometer. It is then dispersed with a 150 l/mm grating in 2nd order and recorded with an intensified charge coupled device (ICCD) camera (camera 1 in Fig. 2, PCO Dicam Pro) with a GaAsP photocathode. This photocathode has a high quantum efficiency of 40 % along the entire spectral range of the emission wavelength of CO (Ångström bands, 450-650 nm). The spectral resolution is 12.8 nm/mm or 0.18 nm/pixel, which leads to an instrumental line width of 0.7 nm in the area of the laser focus (60 μm) or of 1.7 nm with a spectrometer slit width of 140 μm . Due to the wide slit, the limited focal depth along the light sheet or the increasing light sheet thickness along the Rayleigh length did not lead to any or to small intensity losses at most.

The spectrally integrated LIF signal is simultaneously recorded from the opposite side using a second ICCD camera (Camera 2 in Fig. 2; PCO Dicam Pro; S20 photocathode, equipped with a Zeiss $f=100$ mm, $f/2.0$ lens and a bandpass filter range of 470-620 nm, i.e. a combination of Schott Glass filters GG475-2mm and BG38-2mm.

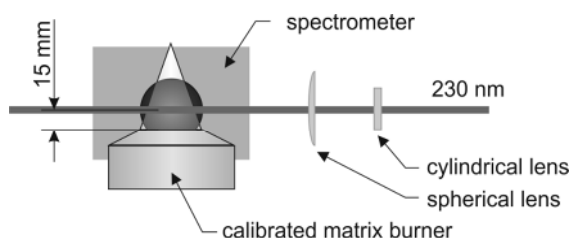


Figure 3: Setup for spectral analysis of the CO fluorescence, side view.

Laminar premixed flames are of high importance in fundamental research. Flow field, gas composition and the temperature profile can be determined with relatively little effort [31]. Furthermore, spatial homogeneity of flames is warranted. High reproducibility and steady combustion are other advantageous features of laminar premixed flames. To produce such a flame, a matrix burner based on a sintered bronze matrix with internal cooling is used. The sintered plate of this burner has a diameter of 60 mm and is equipped with a 5 mm wide shroud gas ring. Through this ring a nitrogen co-flow shields the flame. In rich flames the diffusion of oxygen from the ambient air is thereby prevented. The matrix is internally water cooled with a flow rate of 1 l/min [31]. Both fuel and air are supplied to the matrix burner at room temperature. The mass flow rates are adjusted by means of calibrated mass flow controllers (MKS Multigascontroller 647C). The equilibrium exhaust gas composition is determined by means of GasEq [30].

This burner provides stable premixed laminar methane/air flames (Table 1) which are very homogeneous in radial direction. Figure 4 and Figure 5 present exemplary spectrally integrated CO measurements for the flame at $\Phi=1.45$ (Flame 8 in Table 1). Figure 4 shows an image recorded by camera 2 with an excitation wavelength of 230.105 nm, which corresponds to the CO absorption lines Q(4)-Q(7) ("on"-resonant), near the band head of the B-X (0, 0) transition. The fluorescence signal of CO across the diameter of the burner matrix at 15 mm distance is clearly visible. When the laser wavelength is tuned to 230.16 nm ("off"-resonant), the signal above the burner largely disappears; however some signal remains, in particular close to the left and right boundary of the flame, although rather weak, as indicated by the different intensity levels in Figure 4 and Figure 5. This suggests an additional signal contribution by

other species. The origin of this interfering signal is subject of discussion in a subsequent section on spectrally resolved measurements.

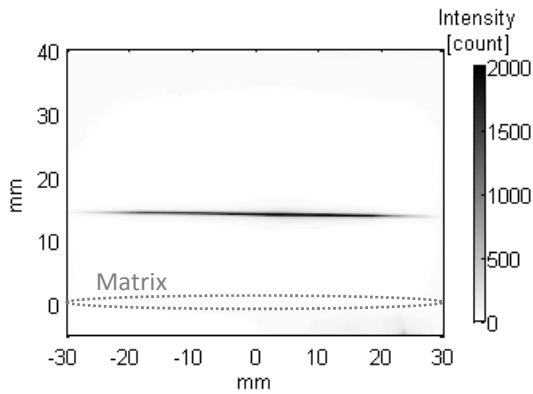


Figure 4: Example image from camera 2 with excitation wavelength of 230.105 nm ("on"-resonant).

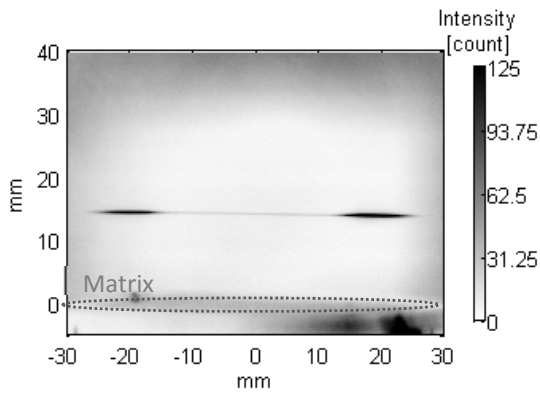


Figure 5: Example image from camera 2 with excitation wavelength of 230.16 nm ("off"-resonant).

In addition to the spectral analysis (below), the dependence of the signal strength on the laser power is investigated in the same flame of equivalence ratio $\phi = 1.45$. A power dependence measurement requires the variation of the laser power without significant alteration of the spatial energy distribution (cf. [32]). To ensure this, a variable attenuator is placed in the beam path. The attenuator is a dielectric mirror, which is optimized for the excitation wavelength of 230.1 nm. It can be tilted relative to the beam path, resulting in a successive variation of the transmission. Thereby, the beam profile is not changed. For each laser power setting, 400 frames are recorded and evaluated. The setup illustrated in Figure 6, makes use of the same light sheet

optics as described in Fig. 3 with difference that the cylindrical lens is rotated by 90°, such that the light sheet is now oriented perpendicular to the matrix to measure the CO profile in the axial/radial plane across the planar height of 15.0 mm. The waist (focus) of the light sheet is located on the flame axis, where it has a height of 10 mm and a thickness of 60 μm with a Rayleigh distance of ± 12 mm. Behind the burner, part of the laser beam (about 5%) is split off by means of a quartz plate, serving as a partially reflecting mirror.

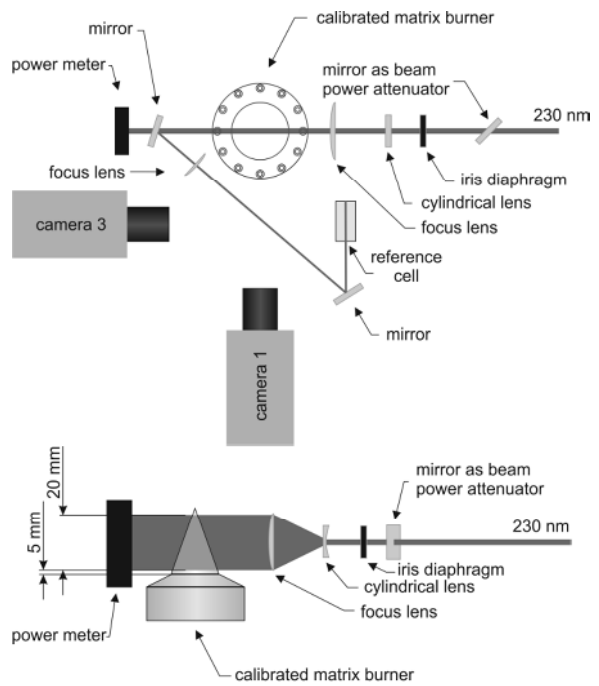


Figure 6: Setup to evaluate the impact of laser power on the signal strength of the CO fluorescence; top and side view.

The focus of the light sheet is 1:1 imaged to a reference cell filled with a solution of Rhodamine 6G (R6G) dye in ethanol using a spherical lens with a focal length of $f = 500$ mm to record the intensity distribution across the light sheet. Behind the quartz plate, a pyroelectric detector (SLT, PEM 20K) is placed to monitor the integral intensity. The measured signal is digitized using an oscilloscope (LeCroy WAVEJET 354).

This combination allows the simultaneous measurement of the absolute pulse energy of the laser and is therefore used to calibrate the intensity distribution in the reference cell. The laser-induced fluorescence of the CO molecules is detected using camera 1 of the spectrometer setup (Fig. 2). To eliminate interference, such as thermal flame luminosity and chemiluminescence, short exposure times of 60 ns are selected. For this purpose, camera 1 is equipped with a fast lens (Zeiss $f=100$ mm, $f/2.0$) and the filter combination previously used for camera 2 (470-620 nm; see Figure 7).

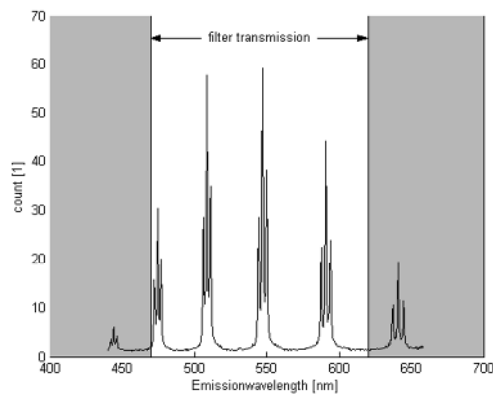


Figure 7: CO emission spectrum and filter transmission.

ICCD camera 3 (LaVision Flame Star II) records the fluorescence of the R6G solution. A long-pass filter (Schott OG550 nm) excludes detection of UV light and the green Nd:YAG wavelength. Furthermore, camera 3 is equipped with a 14 bit AD converter and a Nikkor 135 mm, $f/2.8$ lens.

Two images (“on” and “off”-resonant) are recorded with the CO LIF camera. The differences of the two images then provide the actual fluorescence signal of the resonantly excited CO B-X transition assuming an uniform background contribution of the “on” and “off” excitation wavelength. An example measurement for the atmospheric $\phi = 1.45$ flame (Table 1, No 8) is shown in Figure 8. In addition to the CO fluorescence, the burner surface, creating intense stray

light, can be seen in the images. Because the emission spectrum of CO molecules extends over a wide spectral range, the use of the selected filter results in a high sensitivity, but not a strong selectivity, i.e., discrimination of interfering signals. In the “off”-resonant image such parasitic signal contribution can be observed particularly close to the boundary of the flame, similar to Figure 5. As mentioned above, its origin will be discussed in the Results and Discussion section.

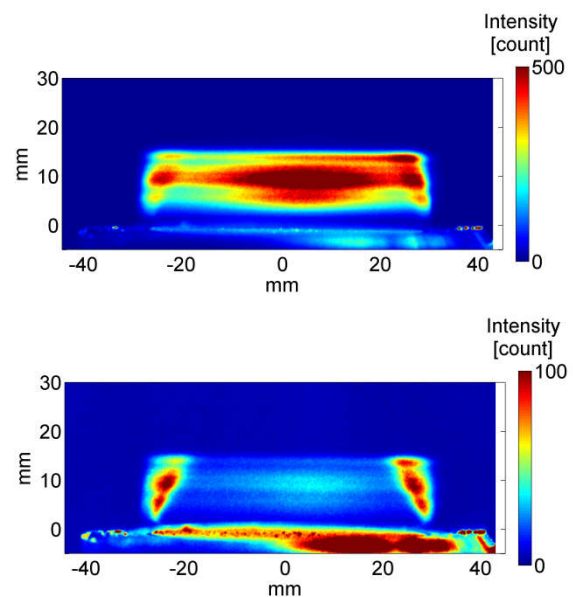


Figure 8: Example measurement in the atmospheric premixed $\Phi=1.45$ flame (Table 1, No 8); top: “on”-resonant image (230.105 nm) bottom: “off”-resonant image (230.16 nm).

Analysis of the CO signal at elevated pressure

To investigate pressure effects on the CO signal and spectral structure, CO PLIF was applied to pressurized laminar premixed flames stabilized in a high pressure environment (Figure 9).

The burner assembly, which can be used to study premixed pressurized flames, has recently been used for soot studies and laser diagnostics development and is described in detail in [33, 34]. It consists of two

concentric water cooled bronze matrices with a cell size of $12\ \mu\text{m}$ (Tridelta Siperam), surrounded by an additional stabilizing air coflow. The diameters of the central matrix, ring matrix, and coflow duct are 41.3 mm, 61.3 mm, and 150 mm, respectively. The burner assembly is mounted in a water-cooled steel pressure housing with full optical access to the premixed flames through thick quartz windows. The pressure inside the housing can be adjusted by throttling the exhaust port with a computer-controlled movable piston. This high pressure housing has also been used for turbulent pressurized flames recently [35].

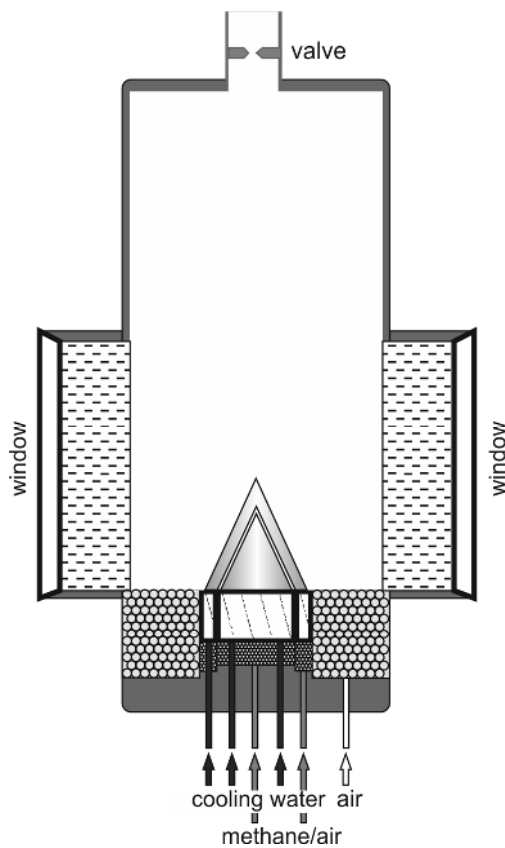


Figure 9: High pressure burner.

Both matrices can be supplied with independently controlled gas mixtures, including different fuels as in [33] or identical fuel at different equivalent ratios for better flame stabilization at increased pressure. Methane for the central and ring matrix, and air for all three in-flows are supplied via in-house calibrated mass flow controllers (Bronkhorst), accurate to better than 1% of

the maximum value. Air and the respective fuel are mixed about two meters upstream of the burner.

For measurements in this burner, the following setup is used (Figure 10).

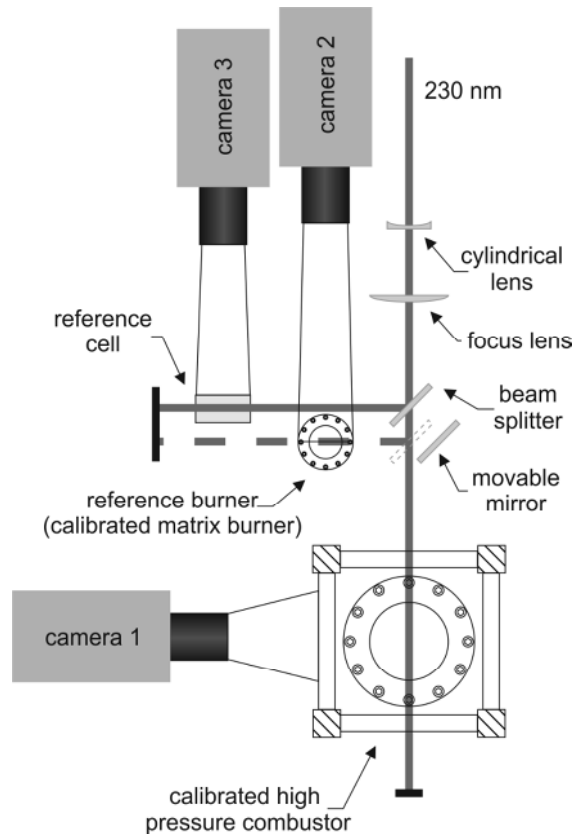


Figure 10: Setup at the high pressure combustor.

The laser beam of wavelength 230.1 nm is expanded into a 10 mm tall light sheet perpendicular to the burner surface, with its axis at a height above burner of 10 mm. For this, the light sheet optics described in the previous calibration section are used. The light sheet can be guided alternatively into the high pressure burner or the reference burner, which is the atmospheric matrix burner described above, by a pneumatically actuated mirror. The reference burner is used to calibrate the CO images of the high pressure burner during post processing. This calibration does not only consist in providing a PLIF signal from a known CO reference concentration, but also takes into account effects of variation of laser fluence across the light sheet and in

the direction of propagation. The latter is caused by the changing width of the beam waist across the burner due to tight focusing. Furthermore, a beam splitter serves to guide a portion of the laser sheet into a reference cell for monitoring of the light sheet with camera 3 as described for the calibration measurements above.

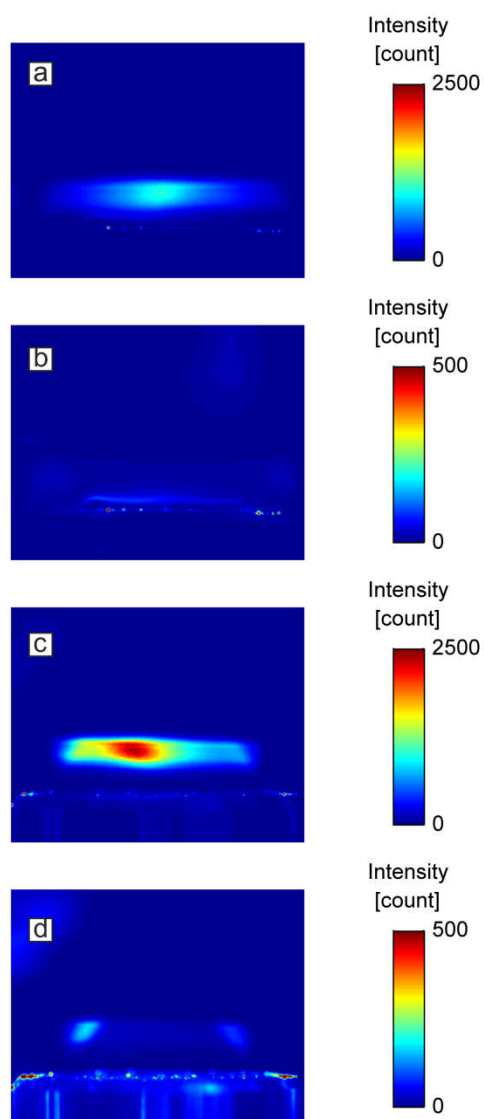


Figure 11: Set of exemplary images recorded for a CO measurement in the high pressure burner: (a) – Image from the high pressure burner “on”-resonant (230.105 nm), (b) – Image from the high pressure burner “off”-resonant (230.16 nm), (c) – Image from the reference burner “on”-resonant, (d) – Image from the reference burner “off”-resonant (note the different intensity scales).

camera 1 described above records the CO PLIF signal emitted from the high pressure flames, and camera 2 (PCO Dicom Pro, S20 photocathode) that from the reference burner. Consequently, the optical path from the last lens of the light sheet optics to the high pressure burner and to the reference burner, respectively, is identical. A full set of measurement consists of four images, which are shown in Figure 11: Two for each burner, in each case one “on”-resonant and one “off”-resonant.

The reference burner is continuously operated at $\Phi=1.4$ (Table 1, No 7) throughout the experiments in the high pressure burner.

Results and discussion

For the interpretation of the measured signals, in particular, with respect to the evidence of interferences from other species mentioned above, spectrally resolved measurements in the atmospheric matrix burner were analyzed.

In Figure 12, spatially resolved emission spectra are compared for two excitation wavelengths. On the left side of the plot the laser is tuned to the CO B-X (0,0) Q(32) rotation line at 230.037 nm (“on”-resonant) and on the right side beyond the band head at 230.16 nm (“off”-resonant). The different intensity ranges represented by the respective color bars should be noted. Also, different horizontal regions in the premixed flames are observed in the two images: “on”-resonant signals were recorded near the center and “off”-resonant in the periphery of the flames. The spectrum shows emission into a wide range of vibrational levels v'' of the A-state; $v''=0$ (445 nm) to $v''=5$ (644 nm) are clearly visible. For each vibrational band, the split of the emission line into the P, Q, and R branches can be observed. To identify potential spectral interferences, the excitation wavelength was

tuned towards longer wavelengths beyond the CO band head, which completely eliminates CO fluorescence. Near the periphery of the flame ($x=15-20$ mm, see Figure 12 top/right) spectral interferences are present. Those are identified as the Swan bands of the C_2 molecule [36]. Figure 12, top, shows that the C_2 emission wavelengths observed near the flame boundary coincide with a wide range of the CO spectrum; therefore, efficient spectral discrimination is possible only at the expense of substantial signal loss. In the case of substantial contributions of spectral interferences, the use of narrowband filters isolating the CO (0,1) or (0,3) vibrational transitions may be an option.

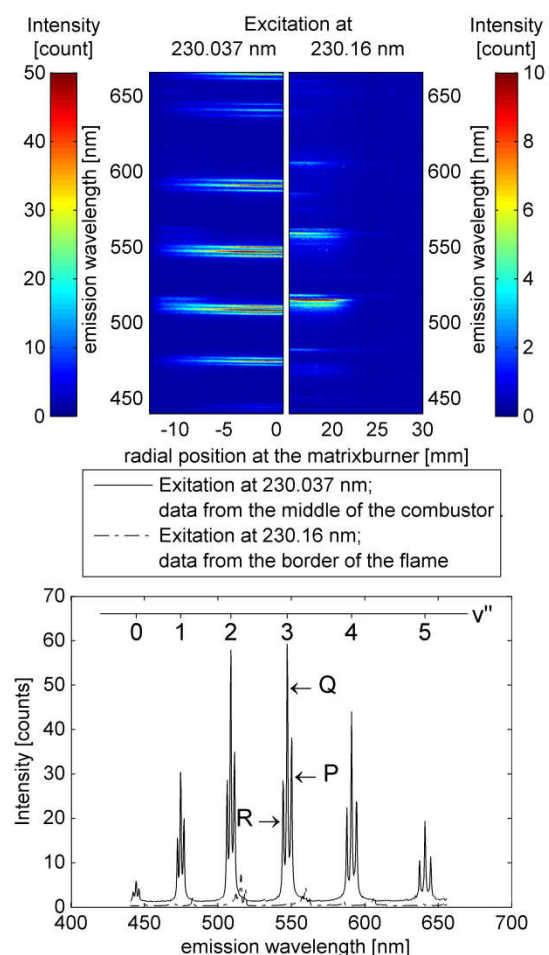


Figure 12: Comparison of emission spectra; top: left: "on"-resonant, right: "off"-resonant; bottom: extracted spectra at the center of the burner (laser "on"-resonant) and the border of the flame (laser "off"-resonant).

If necessary, broadband spectral interference of polycyclic aromatic hydrocarbons (PAH) LIF or laser-induced incandescence can be reduced using a spectral narrowband CO filter which, however, causes a CO signal loss of about 4-5. For our experimental situation this was not required and we could use the high sensitivity of a broad fluorescence filter; no signal increase towards long wavelengths, typical for LII was identified, and potential broad PAH signatures are at or below noise levels as evident from Figure 12.

In another experiment, the signal strength was measured as a function of laser power, with excitation of the Q(4)-Q(7) lines, near the band head, in an atmospheric flame stabilized on the reference burner with $\Phi=1.4$ (Table 1, No 7, Figure 13).

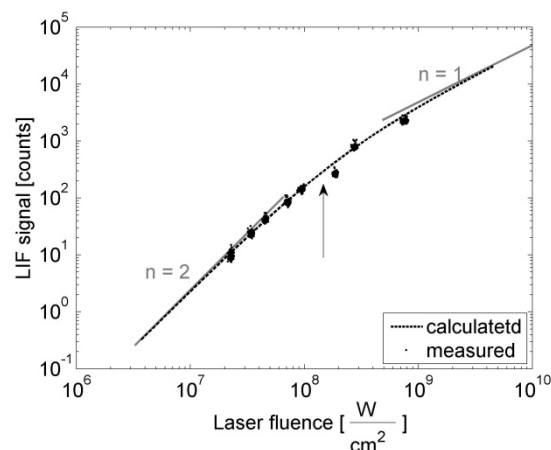


Figure 13: Influence of the laser power on signal strength (measured and calculated); $p=1$ bar, $\Phi=1.4$, $\lambda=230.105$ nm (Table 1, No 7). The arrow at $0.15 \frac{W}{cm^2}$ marks the laser intensity of the planar and spectral resolved CO LIF measurements, unless expressed differently.

Here, the measured data are plotted along with the calculated data according to equations 1 and 2, respectively. For low flux densities ($<1 \cdot 10^8 \frac{W}{cm^2}$) the intensity of the LIF signal is a quadratic function of the laser flux density ($n = 2$). With increasing laser power ionization dominates over quenching and spontaneous emission which leads to a linear relationship ($n = 1$) between laser flux density

and LIF signal ($>10^9 \frac{W}{cm^2}$). For planar measurements this linear regime implies the positive effect of a CO detection independent of the local laser fluence or light sheet thickness. When using the spectrally integrated 2-photon cross section of Di Rosa [14] with $\sigma_0^{(2)} = 1.5 \cdot 10^{-35} \pm 0.7 \text{ cm}^4$, or the more recent value of Carrivain [29] with $\sigma_0^{(2)} = 2.25 \cdot 10^{-35} \pm 0.5 \text{ cm}^4$, the saturation of the 2-photon transition by depopulation of the ground state is achieved at significantly higher laser flux densities ($>10^{11} \frac{W}{cm^2}$). A measured excitation scan in a flame at 1 bar (Table 2, flame #1), along with a simulated spectrum as described in the Theory section, is shown in Figure 14. The only parameters fitted to the experimental spectrum are rotational temperature, the spectral line shape of the laser, and the total intensity.

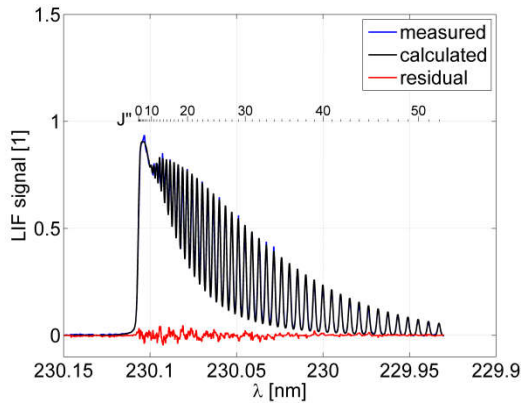


Figure 14: Excitation spectrum (measured and calculated) at 1 bar (Table 2, No 1). The rotational quantum numbers J'' of the Q branch are marked.

The spectra are in excellent agreement, in terms of both line positions and intensities. The fitted rotational temperature of 1870 K is in good agreement with the measured CARS temperature of 1913 K [31]. The latter atmospheric flame is the most similar flame to the examined flame in the high-pressure burner with respect to the equivalence ratio and gas velocities.

To investigate the J-dependent photoionization in more detail, spectra were

recorded with higher laser intensities up to 0.6 GW/cm^2 . Figure 15 shows the CO band head for the increased photon flux density in more detail. The increased photoionization in the range of $J=8-12$, directly next to the band head, is reflected by an intensity drop.

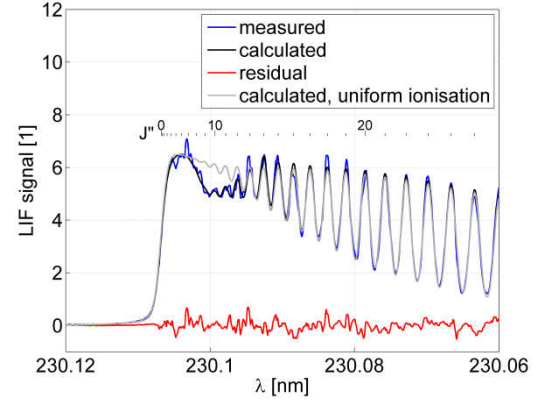


Figure 15: Influence of the J-dependent photoionization on the LIF spectrum. The laser intensity of 0.6 GW/cm^2 is four times higher than for the spectra shown in Fig. 14.

To determine the relative photoionization cross section, additionally the low-pressure CO LIF excitation spectrum recorded by Koch et al. [37] at 0.3 mbar, 420 K and a laser intensity of about 1 GW/cm^2 was employed. Under these conditions (low pressure and high photon flux) essentially only photoionization contributes to the depletion of the excited state population (see equation 4). To reproduce the experimental flame and low-pressure spectra, the cross sections $\sigma_i^{J'}$ of $J'=8-12$ have to be increased compared to the J' -averaged value $\sigma_i^{avg} = 1.0 (\pm 0.3) \cdot 10^{-17} \text{ cm}^2$ given in [11] for $J'=0-8$ and 12. Fitting the missing values for $J'=9-11$ to the power dependent spectra, the cross sections especially for $J'=9$ and $J'=10$, $\sigma_i^9 = 1.6 (\pm 0.3) \cdot \sigma_i^{avg}$ and $\sigma_i^{10} = 1.4 (\pm 0.3) \cdot \sigma_i^{avg}$, are substantially higher than the J' -averaged value. A hint for this behaviour can be found in [38]. The excitation wavelength of this CO B-X (0,0) Q(9) 2-photon transition at 230.1005 nm corresponds quite exactly to the CO^+ B-X (0,1) P(8) transition, which can be reached with 2+1+1 multi-photon absorption

[38]. For our purpose of quantitative CO 2P-PLIF measurements, the increased ionisation cross section can be used to estimate the local laser flux density for the respective experimental situation.

Such excitation spectra were also recorded at 3 and 5 bar and can also be compared with the simulation, using the line shape and shift parameters mentioned above [12]. In Figure 16, measurement and calculation are shown for a 5 bar case as an example.

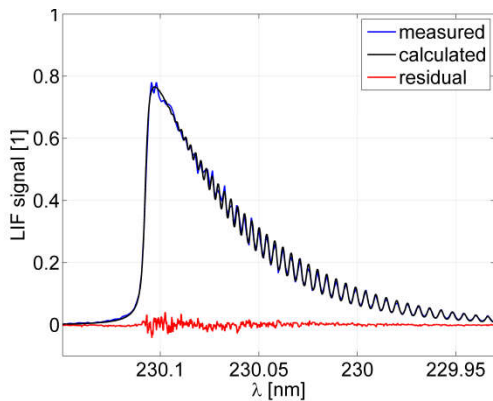


Figure 16: Excitation spectra at 5 bar (Table 2, No 8); intensities scaled to those of the spectrum at 1 bar (Figure 14).

In these spectra, good agreement between measurement and calculation is achieved again. Similar to the NO A-X transition [39], the pressure shift of the considered CO B-X transition lines of about $(-1/3)$ of the pressure broadening [12] indicates an asymmetric pressure broadening line profile, driven by the van der Waals interaction between CO and the dominant collider. As for the NO A-X band system [39], also here in case of the CO B-X system [40, 41] the asymmetry of homogeneous line profile can be adequately described by a Lindholm profile [28] at room temperature and elevated pressures. Only the long-wavelength (red) side of the blue-degraded band head is very sensitive to the line shape asymmetry described above. With increasing temperature, the asymmetry decreases, proportional to $T^{-1.3}$ [39]. At a flame temperature of about 1900 K, no asymmetry

could be found within the measurement accuracy, and the use of a Lorentz profile delivers the best results (see Figure 16).

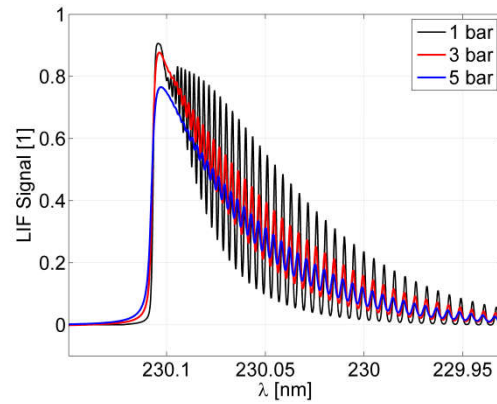


Figure 17: Calculated excitation spectra at different pressures. In the calculation of the shown LIF spectra, the CO mole fractions, the temperatures of 1870 K and the laser intensity of 0.15 GW/cm^2 were kept constant.

The simulated excitation spectra in Figure 17 illustrate the impact of varying pressure on spectral structures. While the spectrum line width at 1 bar is dominated by the Doppler width (0.5 cm^{-1} at 1900 K) in relation to the pressure broadening (0.18 cm^{-1}) and laser width (0.1 cm^{-1}), pressure broadening with 0.9 cm^{-1} dominates the line shape at 5 bar. Also, a line shift of $0.075 \text{ cm}^{-1}/\text{bar}$ towards high wavelength is observed with increasing pressure. These values are in good agreement with those of [13], so that their model and coefficients of pressure broadening and pressure shift are considered in the further calculations. In the comparative calculations of the LIF spectra shown in Figure 17 the CO mole fraction and temperature were kept constant, according to the experimental boundary conditions of the measured spectra shown in Figure 14 and Figure 16. Both the CO number densities as well as the quenching rates scale with respect to pressure, so the total LIF intensity is constant. In addition, as the pressure increases, the contribution of ionization losses to the quantum yield becomes less important, see equation (4). Therefore the intensity maxima of the

overlapping lines near the band head are nearly independent from pressure, and only drop little with increasing pressure. On the other hand, intensity maxima of more isolated lines ($J > 45$) substantially decrease with increasing pressure due to the dominant pressure broadening for pressures $p > 3$ bar.

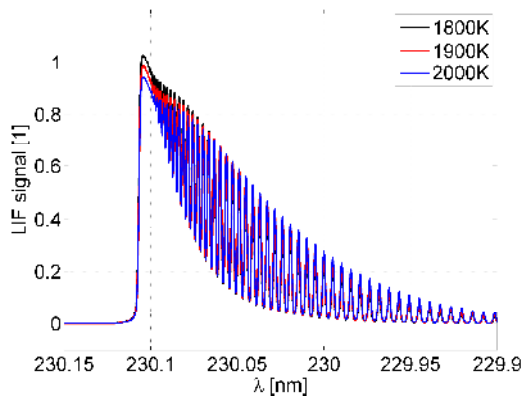


Figure 18: Calculated excitation spectra at different temperatures. The calculations are done for atmospheric pressure and constant CO concentration.

In addition to pressure broadening the influence of temperature on signal intensity must be also taken into account [7]. Figure 18 illustrates the dependence of the shape of the excitation spectrum on temperature. However, the use of the described diagnostics in turbulent flames does not provide the local temperature. Therefore, the selection of an excitation line with little temperature dependency due to ground state population, line broadening and quenching is an option under those conditions.

Figure 19 indicates that the signal strength towards the band head increases for low temperatures, while for shorter wavelengths the ratio is reversed, showing a slight increase of signal with temperature. In general, the signal intensity dependence on temperature is relatively weak for higher J . Therefore, a suitable transition with weak dependence of ground state population on temperature can be selected, if the approximate temperature range of a flame can be estimated. In the

exemplary temperature range shown in Fig. 18 this is line Q(26), but at the expense of reduced intensity and hence decreased sensitivity compared to excitation near the band head.

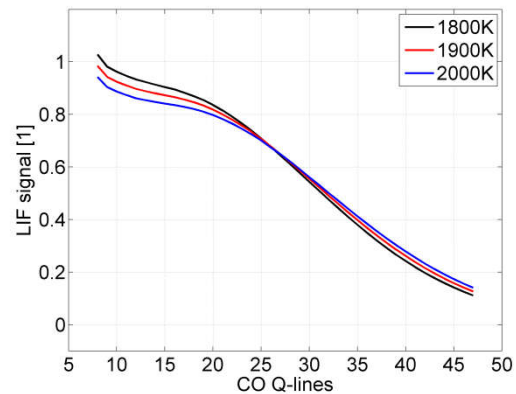


Figure 19: Intensities of different CO lines of the calculated excitation spectrum at different temperatures to select a temperature insensitive line.

In the reference burner, measurements were carried out at various methane-air ratios. The high pressure burner was used to study pressure as additional parameter. In both sets of measurements, the CO concentration is determined by calibration using the atmospheric flame at $\Phi=1.45$ as reference. For this flame, the CO equilibrium concentration is calculated via GasEq [30]. In the high pressure burner, the nominally same flame can be investigated; because of identical CO concentrations for both burners, the sensitivity ratio between the two different detection pathways, due to different cameras, lenses, and attenuation of signal and laser power by windows, can be determined. Table 1 and Table 2 summarize the test conditions investigated for both burners.

CO on-resonant images are generally corrected for background and C_2 interferences using the respective off-resonant images (Figure 20). The ratio of those corrected CO images serves to derive the sensitivity ratio of both detection systems when applied to the nominally same flames in both burners (Figure 21).

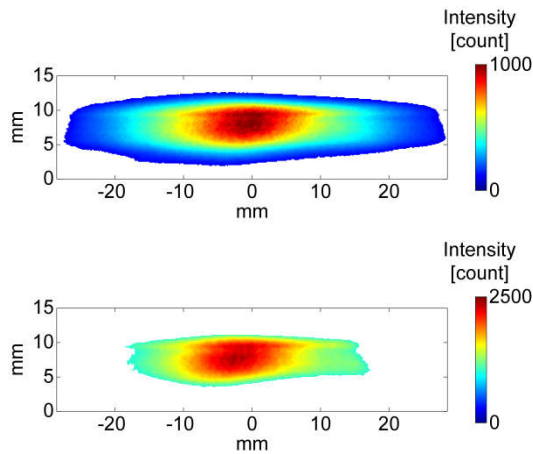


Figure 20: Deduction of the sensitivity ratio of both detection systems: CO images corrected for background and C₂ interference, high pressure burner (top) and reference flame (bottom) at 230.105 nm.

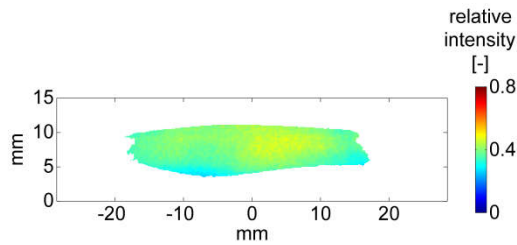


Figure 21: Spatially resolved sensitivity ratio of both detection systems, that for high pressure flames and that for the reference flame, respectively.

To calibrate other flames stabilized in the high pressure burner, the corrected CO images are multiplied by the sensitivity ratio of both detection systems, as described above.

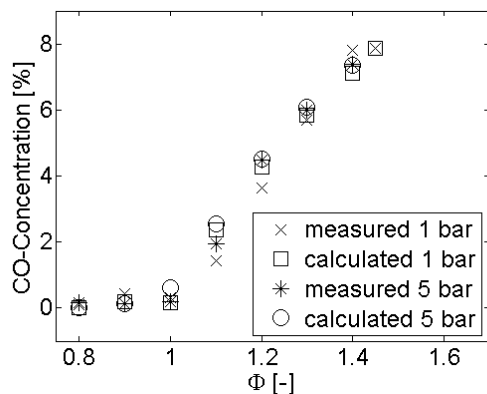


Figure 22: Measured CO concentrations at 1 and 5 bar (flames see Table 1 and Table 2) in comparison to equilibrium concentrations calculated with GasEq [30]. The measurements were taken with a laser wavelength of 230.105 nm on the burner axis at a height of 10 mm above the burner exit.

Measured CO mole fractions in the high pressure burner are compiled in Figure 22 for different equivalence ratios and for two pressures. Values from an equilibrium calculation [30] are shown for comparison. The agreement is generally very good for both equivalence ratio and pressure variations. It should be noted that CO concentrations are given here in terms of mole fractions, although the LIF signal is proportional to number density. Consequently, at higher pressure, the LIF signal at constant mole fraction should increase due to higher density. However, at the same time increasing density leads to an increase of the collisional quenching rate Q_{elec} according to Eq. 7 by the same factor, as long as quenching is the dominating loss channel for the excited state population. Therefore, these two effects cancel and allow a comparison of signals on the basis of mole fractions rather than densities.

The signal-to-noise-ratio (SNR) for an average image obtained from 100 single pulse images in the reference burner is around one at equivalence ratios between 0.8 and 0.9. The calculated CO concentration at $\Phi = 0.9$ is 200 ppm, which represents the detection limit for averages of 100 single-pulse measurements. For instantaneous images the detection limit is 1000 ppm. In the high pressure burner the SNR is lower due to losses at the windows. In this case, the detection limit is 1000 ppm at 5 bar for an average of 100 instantaneous images.

Possible sources of uncertainty

The CO concentration is calibrated using a reference flame with known CO concentration. An error in this reference concentration propagates linearly into the measurement in the test system. The specified precision of the mass flowmeters for the reference flame is 3 % for methane and 4 %

for air, respectively. The resulting uncertainty of the equivalence ratio transforms to an uncertainty of up to 20 % of the CO concentration.

Another possible uncertainty results from fluctuations of the laser fluence during the test series. Typical fluence fluctuations of below 2 % result in an uncertainty of up to 14 % in the CO concentration.

The relative population of the rotational and vibrational state involved in the probed transition depends on local temperature. In the atmospheric reference burner the latter was measured with CARS [31], while it is unknown in the high pressure burner. This yields an additional uncertainty of up to 10 %.

In addition, the different fluorescence quantum yield due to different degree of

photoionization (see Figure 13) leads to a systematic error of 10-20%. Altogether, this results in a global uncertainty of about 30 %.

Flame No	Pressure p [bar]	Φ	CH ₄ [sl/min]	Air [sl/min]
1	1	0.8	1.733	20.63
2	1	0.9	3.42	36.18
3	1	1.0	1.733	16.5
4	1	1.1	2.55	22
5	1	1.2	2.55	20.2
6	1	1.3	2.05	15
7	1	1.4	1.733	11.8
8	1	1.45	2.287	15

Table 1: Flame settings for the investigated atmospheric flames stabilized on the matrix burner; flow rates refer to standard conditions at 1.013 bar and 273 K.

Flame No	Pressure p [bar]	Φ_{inner}	Inner flame			Φ_{ring}	Ring flame			Coflow
			CH ₄ [sl/min]	Air [sl/min]	v_{inner} [cm/s]		CH ₄ [sl/min]	Air [sl/min]	v_{ring} [cm/s]	Air [sl/min]
1	1	1.4	1.25	8.54	13	1.0	2.08	19.87	28	60
2	5	0.8	4.08	48.66	14	1.0	6.32	60.33	17	215
3	5	0.9	4.54	48.19	14	1.0	6.32	60.33	17	214
4	5	1.0	5.00	47.74	14	1.0	6.32	60.33	17	209
5	5	1.1	5.45	47.29	14	1.0	6.32	60.33	17	207
6	5	1.2	5.89	46.85	14	1.0	6.32	60.33	17	201
7	5	1.3	6.32	46.42	14	1.0	6.32	60.33	17	198
8	5	1.4	2.89	19.71	6	1.0	6.32	60.33	17	197

Table 2: Flame settings for the investigated flames in the high pressure burner; flow rates refer to standard conditions at 1.013 bar and 273 K

Measurements in atmospheric non-premixed swirled methane / air flames

While the previous sections described the development and detailed characterization of the measurement technique in matrix burners at atmospheric and increased pressure, this section describes the application to a generic model combustion chamber to assess its potential under technically relevant

conditions. The swirl-stabilized model combustor, described in detail in [42, 43] uses an annular methane gas flow which is entrained between two swirling air flows (cf. Figure 23). The combustor has a square cross section of 85 mm width and a height of 114 mm. 2 mm thick fused silica side windows mounted between steel rods in the corners allow for excellent optical access. The combustor exit contracts into a cylindrical outlet with 40 mm inner diameter. This burner configuration allows optical access from all four sides, and almost the entire combustion

chamber volume can be optically accessed. In Figure 23, the in-plane components of the velocity field in the model combustor are shown for a flame with an equivalence ratio of $\Phi = 0.75$ and a thermal output of 10 kW [42]. The strong inner recirculation zone (iRZ) near the combustor axis reflects the typical flow pattern of a swirl-stabilized flame. The iRZ extends from the central air nozzle approximately 60 mm downstream. Furthermore, an outer recirculation zone (oRZ) forms in the outer part of the combustion chamber. The velocities in the oRZ are low. The oRZ extends from the burner head plate to a height of approximately 10 mm.

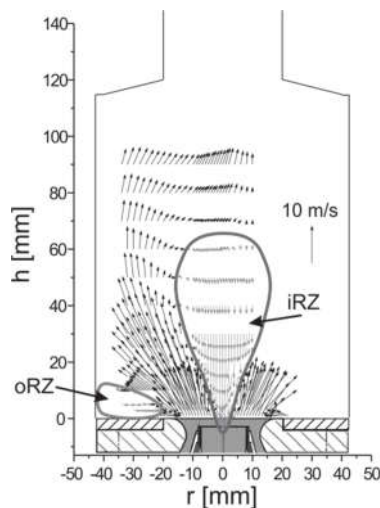


Figure 23: Velocity field of the model combustor (in-plane components, $\Phi=0.75$) [43]

For the CO measurements, flames with a constant thermal output of 10 kW were used. Although the equivalence ratio of the presented flame deviates, the similarity of the flow fields will be high enough for the qualitative discussion. In order to capture the entire combustion chamber with a light sheet of 10 mm height, the CO measurements were carried out at six different heights above the burner head plate. The upstream edge of the light sheet closest to the injector is flush with the burner head plate.

In Figure 24, the CO concentration distribution for a flame with a thermal output of 10 kW and $\phi = 1.3$ is represented. With the same thermal output the velocity field is qualitatively similar. Additionally the deconvoluted OH chemiluminescence is superimposed as contour plot. It serves as a spatially resolved heat release indicator. While CO is formed in the lowest plane due to chemical reactions, higher CO concentrations in the second plane are attributed to the iRZ. Here, CO is recirculated back from rich regions towards the burner head plate. The decrease in CO concentrations in the third plane is caused by oxidation in the flame zone. This relationship is demonstrated in the superposition of the chemiluminescence images and the CO LIF images. The three measurement positions furthest from the burner face exhibit nearly constant concentrations of CO, because insufficient oxygen concentrations prevent its further oxidation.

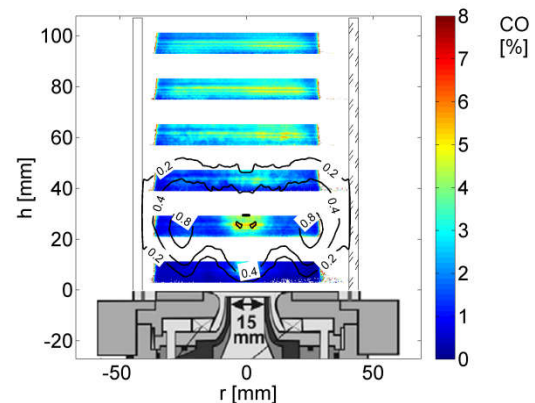


Figure 24: CO-LIF (color map) and chemiluminescence, symmetrized and deconvoluted (contour plot) images for $\Phi=1.3$. CO LIF was measured with a laser wavelength of 230.105 nm.

The reference flame in the matrix burner is narrower than the model combustor. Due to the lack of reference signal at larger radii, CO concentrations close to the window surfaces were not derived.

Characteristic of the measured flame is a conical reaction zone with a swirl-dependent

opening angle, which encloses an extended recirculation area. This recirculation extends to the injector outlet for the presented burner. For the investigated burner, comprehensive data on flow field, temperature and mixture fraction distribution under similar conditions [43] are available. Using these data, the structure of the CO distribution measured here and its behavior as a function of the stoichiometry can be interpreted.

Figure 24 also shows the position of the flame zone using Abel-transformed OH chemiluminescence. Under lean conditions, the reaction zone concentrates in a region close to the injector, where turbulent mixing has produced rapidly flammable mixtures. In the downstream recirculation region, a spatially relatively homogeneous CO distribution is observed for the studied stoichiometry. In this area, residence times are sufficiently long to establish CO concentrations according to the equilibrium conditions at the global stoichiometry. The calculated CO volume fraction is 6% for $\Phi = 1.3$ according to an adiabatic equilibrium calculation using GasEq [30]. The measured values of 5% CO thus agree well, given the uncertainty about the deviation of the actual temperature from the adiabatic temperature assumed in the equilibrium calculation. The high CO values typically correlate to high mixture fractions [44] in or near the reaction region. The increase in the CO volume fraction can be qualitatively explained by the increase of the mixture fraction near the injector on the burner axis. For similar flames on the same burner, mixture fraction distributions were measured using Raman scattering by Weigand et al. [43] and clearly show a higher mixture fraction in the vicinity of the injector. This results in correspondingly higher CO concentrations. In the immediate vicinity of the flame axis, however, the mixture fraction decreases due to the recirculated leaner

burned mixtures, which explains the small minimum of the CO concentration in the second measurement area above the injector. The same research group of W. Meier et al. [45] determined the CO concentration at the height of 5 mm above the burner exit using Raman measurements. Their measurements show CO maxima in the IRZ and the ORZ, which are also present in measurement area directly above the fuel injector of Figure 24.

Summarizing the results of the swirled methane/air flame experiments the measured CO concentration shown in Figure 23 correlates well with the results of the Raman measurements of mixture fraction [43] and of the CO concentration [45] in the vicinity of the burner exit. In addition, the planar CO LIF technique enables an efficient concentration measurement within the entire combustion chamber.

Summary and Outlook

In order to develop a quantitative 2-photon PLIF measurement technique for CO, experiments were first performed under well-controlled conditions in a premixed laminar atmospheric burner with excitation wavelengths close to 230 nm in the Hopfield-Birge system ($B^1\Sigma^+ \leftarrow X^1\Sigma^+$) with resulting fluorescence in the Ångström bands of the $B^1\Sigma^+ \rightarrow A^1\Pi_u$ transition in the visible range (450-670 nm). This burner served as a source for well-defined CO reference concentrations for calibration of CO PLIF signals in further test systems. The LIF signal was analyzed with a spectrometer, and possible interferences from C_2 Swan bands were identified under certain circumstances. This observation may necessitate improved spectral filtering strategies while maintaining sufficient signal levels.

In the next step, the measurement technique was tested in a laminar premixed flame at elevated pressure. Implications of pressure on

detection limits, electronic quenching and spectral line widths and positions, respectively, were discussed, the latter with the help of simulated spectra. Finally, the quantitative, planar measurement technique was demonstrated in an atmospheric generic combustion chamber with turbulent swirl-stabilized flames, as a first step towards application in a gas turbine combustor operating under realistic conditions. In this configuration the measurement technique is mainly useful for quantitative measurements of averaged concentrations. Single shot CO LIF images can mainly be used qualitative analysis. To achieve quantitative single pulse measurements the setup needs to be optimized further to increase the selectivity and the sensitivity, for example with a narrowband spectral fluorescence filter and a multi-color detection system, i.e. a dual camera system for separate detection of both CO and interfering spectral features. Such a filter and camera system could substantially

reduce spectral interferences of C₂ LIF, but only at the expense of signal loss. So the measurement strategy differs depending on the experimental task, to overcome the tradeoff between selectivity and sensitivity.

The obvious next logical step is to test the measurement system in a combustion test rig with realistic flow, temperature and pressure conditions relevant to aircraft engines [46].

Acknowledgement

We would like to thank Martin Müller for his help to set up the experiments. Dr Eggert Magens is acknowledged for stimulating discussions and valuable suggestions. We would like to thank gratefully Dr. Ulrich Meier for his comments on the manuscript. This work has been funded by the DLR Directorate of Aeronautics through the project LOCCA (Low NO_x Oxide Ceramic Combustor for Aero-Engines).

References

1. ICAO, Environmental Protection, Annex 16 to the Convention on International Civil Aviation, Vol. II: Aircraft Engine Emissions, ISBN 978-92-9231-123-0 (2008)
2. A.C. Eckbreth: Laser Diagnostics for Combustion Temperature and Species (Gordon and Breach, Amsterdam, 1996)
3. K. Kohse-Höinghaus, J.B. Jeffries, (eds.): Applied Combustion Diagnostics (Taylor and Francis, New York, 2002)
4. P.H. Krupenie: The Band Spectrum of Carbon Monoxide (National Standard Reference Data Series - National Bureau of Standards - 5 (NSRDS-NBS 5), U.S. Dept. of Commerce, Washington, DC, 1966)
5. K.P. Huber, G. Herzberg: Molecular Spectra and Molecular Structure IV, Constants of Diatomic Molecules (Van Nostrand, New York, 1979)
6. B.J. Kirby, R.K. Hanson: Appl. Phys. B: **69**, 505-507 (1999)
7. B.J. Kirby, R.K. Hanson: Proc. Combust. Inst. **28**, 253-258 (2000)
8. B.J. Kirby, R.K. Hanson: Appl. Opt. **41**, 1190-1201 (2002)
9. G.W. Loge, J.J. Tiee, and F.B. Wampler: J. Chem. Phys. **79**, 196–202 (1983)
10. M.S. Alden, S. Wallin, and W. Wendt: Appl. Phys. B **33**, 205–208 (1984)
11. M.D. Di Rosa, R.L. Farrow: J. Opt. Soc. Am. B **16**, 861-870 (1999)
12. M.D. Di Rosa, R.L. Farrow: J. Quant. Spectrosc. Rad. Trans. **68**, 363-375 (2001)
13. T.B. Settersten, A. Dreizler, R.L. Farrow: J. Chem. Phys. **117**, 3173-3179 (2002)
14. M.D. Di Rosa, R. Farrow: J. Opt. Soc. Am. B **16**, 1988-1994 (1999)

15. J. Rosell, J. Sjöholm, M. Richter, M. Aldén: *Appl. Spectrosc.*, **67**, 314-320 (2013)
16. B. Li, X. Li, D. Zhang, Q. Gao, M. Yao, Z. Li: *Opt. Express* **25**, 25809–25818 (2017)
17. D.R. Richardson, S. Roy, and J.R. Gord: *Opt. Lett.* **42**, 875–878 (2017)
18. K.A. Rahman K.S. Patel, M.N. Slipchenko, T.R. Meyer, Z. Zhang, Y. Wu, J.R. Gord, S. Roy: *Appl. Optics* **57**, 5666-5671 (2018)
19. J. M. Seitzman, J. Haumann, R.K. Hanson: *Appl. Opt.* **26**, 2892-2899 (1987)
20. R.P. Saxon, J. Eichler: *Phys. Rev. A* **34**, 199-206 (1986)
21. R. Loudon: *The Quantum Theory of Light*, (Clarendon, Oxford, 1983)
22. D.J. Bamford, L.E. Jusinski, W.K. Bischel, *Phys. Rev. A.* **34**, 185–198 (1986)
23. B. Atakan, J. Heinze, U.E. Meier: *Appl. Phys. B* **64**, 585–591 (1997)
24. A.O. Vydrov, J. Heinze, M. Dillmann, U.E. Meier, W. Stricker: *Appl. Phys. B* **61**, 409-414 (1995)
25. A. Le Floch: *Mol. Phys.* **72**, 133-144 (1991)
26. M. Eidelsberg, J.-Y. Rocin, A. Le Floch, F. Launay, C. Letzelter, J. Rostas: *J. Mol. Spectr.* **121**, 309-336 (1987)
27. P.J.H. Tjossem, K.C. Smyth: *J. Chem. Phys.* **91**, 2041-2048 (1987)
28. E. Lindholm: *Ark. Mat. Astr. Fys.* **32A**, 1-18 (1945)
29. O. Carrivain, M. Orain, N. Dorval, C. Morin, G. Legros: *Appl. Spectrosc.*, **71**, 2353-2366 (2017)
30. C. Morley, GASEQ-A Chemical Equilibrium Program for Windows (2018)
<http://www.c.morley.dsl.pipex.com/>
31. P. Weigand, R. Lückcrath, W. Meier, Documentation of flat premixed laminar CH₄/Air standard flames: Temperatures and species concentrations (2018)
http://www.dlr.de/vt/desktopdefault.aspx/tabid-3065/4632_read-6696/
32. S. Linow, A. Dreizler, J. Janicka, E.P. Hassel: *Appl. Phys. B* **71**, 689-696 (2000)
33. K.P. Geigle, Y. Schneider-Kühnle, M.S. Tsurikov, R. Hadeff, R. Lückcrath, V. Krüger, W. Stricker, M. Aigner: *Proc. Combust. Inst.* **30**, 1645-1653 (2005)
34. J. Heinze, U. Meier, T. Behrendt, C. Willert, K.P. Geigle, O. Lammel, R. Lückcrath: *Z. Phys. Chem.* **225**, 1315-1341 (2011)
35. K.P. Geigle, M. Köhler, W. O’Loughlin, W. Meier: *Proc. Combust. Inst.* **35**, 3373-3380 (2015)
36. M.D. Cooper, R.W. Nicholls: *J. Quant. Spectrosc. Radiat. Transfer.* **15**, 139-150 (1975)
37. U. Koch, J. Riehmer, B. Esser, A. Gülhan, *Proc. 6th European Symp. on Aerothermodynamics for Space Vehicles*, Versailles, France, 3–6 November 2008 (ESA SP-659, January 2009)
38. F. Di Teodoro, R. L. Farrow, *J. Chem. Phys.* **114**, 3421-3428 (2001)
39. A. Y. Chang, M. D. Di Rosa R. K. Hanson: *J. Quant. Spectrosc. Radiat. Transfer* **47**, 375-390 (1992)
40. O. Carrivain: Thèse de doctorat, Université Pierre et Marie Curie, 2015
41. A.O. Vydrov, J. Heinze, U.E. Meier: *J. Quant. Spectrosc. Radiat. Transfer* **53**, 277-287 (1995)
42. R. Giezendanner, O. Keck, P. Weigand, W. Meier, U. Meier, W. Stricker, M. Aigner: *Combust. Sci. Technol.* **175**, 721-741 (2003)
43. P. Weigand, W. Meier, X.R. Duan, W. Stricker, M. Aigner: *Combust. Flame* **144**, 205-224 (2006)
44. J. Warnatz, U. Maas, R.W. Dibble: *Combustion* (Springer, Berlin Heidelberg New York, 2006)
45. W. Meier, X.R. Duan, P. Weigand: *Combust. Flame* **144**, 225-236 (2006)
46. L. Voigt, J. Heinze, T. Aumeier, T. Behrendt, F. di Mare: *Proc. ASME Turbo Expo 2016: Turbomachinery Technical Conference and Exposition*, Paper Number GT2016-63413, June 26-30, 2017, Charlotte, NC, USA